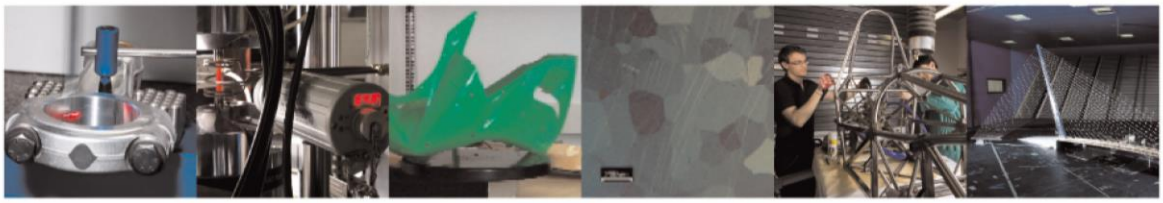

# In-Process Monitoring of Selective Laser Melting: Spatial Detection of Defects Via Image Data Analysis

Grasso, MARCO LUIGI; Laguzza, Vittorio; Semeraro, Quirico; Colosimo, BIANCA MARIA

This is a post-peer-review, pre-copyedit version of an article published in JOURNAL OF MANUFACTURING SCIENCE AND ENGINEERING, 139/5, on November 10, 2016. The final authenticated version is available online at: https://doi.org/10.1115/1.4034715

https://asmedigitalcollection.asme.org/manufacturingscience/article/doi/10.1115/1.4034715/377587/InProcess-Monitoring-of-Selective-Laser-Melting

# In-process Monitoring of Selective Laser Melting: Spatial Detection of Defects via Image Data Analysis

**Marco Grasso**[1]
Dipartimento di Meccanica, Politecnico di Milano
Via La Masa 1, 20156 Milan (Italy)
marcoluigi.grasso@polimi.it

**Vittorio Laguzza**
Dipartimento di Meccanica, Politecnico di Milano
Via La Masa 1, 20156 Milan (Italy)
vittorio.laguzza@polimi.it

**Quirico Semeraro**
Dipartimento di Meccanica, Politecnico di Milano
Via La Masa 1, 20156 Milan (Italy)
quirico.semeraro@polimi.it

**Bianca Maria Colosimo**
Dipartimento di Meccanica, Politecnico di Milano
Via La Masa 1, 20156 Milan (Italy)
biancamaria.colosimo@polimi.it

## ABSTRACT

*Selective laser melting (SLM) has been attracting a growing interest in different industrial sectors as it is one of the key technologies for metal additive manufacturing. Despite of the relevant improvements made by the SLM technology in the recent years, process capability is still a major issue for its industrial breakthrough. As a matter of fact, different kinds of defect may originate during the layer-wise process. In some cases, they propagate from one layer to the following ones leading to a job failure. In other cases, they are hardly visible and detectable by inspecting the final part, as they can affect the internal structure or structural features that are difficult to measure. This implies the need for in-process monitoring methods able to rapidly detect and locate defect onsets during the process itself. Different authors have been investigating machine sensorization architectures, but the development of statistical monitoring*

[1] Corresponding author; Tel.: (+39) 0523-623190, Fax: (+39) 0523-645268

*techniques is still in a very preliminary phase. This paper proposes a method for the detection and spatial identification of defects during the layer-wise process by using a machine vision system in the visible range. A statistical descriptor based on Principal Component Analysis (PCA) applied to image data is presented, which is suitable to identify defective areas of a layer. The use of image k-means clustering analysis is then proposed for automated defect detection. A real case study in SLM including both simple and complicated geometries is discussed to demonstrate the performances of the method.*

*Keywords: Additive Manufacturing; Selective Laser Melting; Process Monitoring; Image Analysis; Principal Component Analysis; k-means Clustering*

## 1 INTRODUCTION

Additive manufacturing (AM) of functional parts via selective laser melting (SLM) has been attracting an increasing interest in industry in the recent years [1 – 7]. The SLM technology involves the use of a laser to locally melt a metal powder bed on a layer-by-layer basis, to produce parts whose structural properties and shape complexity prevent from the use of conventional processes. The high potential provided by this technology has been paving the way to innovative applications in different domains, e.g., aerospace, bio-medical, tooling and moulding, and automotive [1; 8 - 10].

SLM belongs to the so-called “powder bed fusion” processes. A thin layer of metal powder (e.g., average thickness of about 50 μm) is deposited on a flat substrate via a powder deposition system. Then, the laser melts the powder to realize the first slice of the part by following a predefined scanning path. When the scan of the first layer is complete, the substrate is lowered, a new layer of powder is deposited and the process is repeated to realize the following slice. For a more detailed description and overview of the SLM technology, the reader may refer to Gibson et al. [1]. Despite of great

improvements of SLM systems in the recent years, the process capability still represents a major limitation to their industrial breakthrough. The quality of the part depends on hundreds of controllable parameters, but it is also affected by many nuisance factors. Local defects may occur during the laser scanning of one (or more) layers, caused by improper process parameters or supporting strategies, wrong powder deposition, possible material contamination, etc. [11 - 12]. Furthermore, different features are known to be critical, like overhang (i.e., down-facing) structures and acute corners [13 – 15].

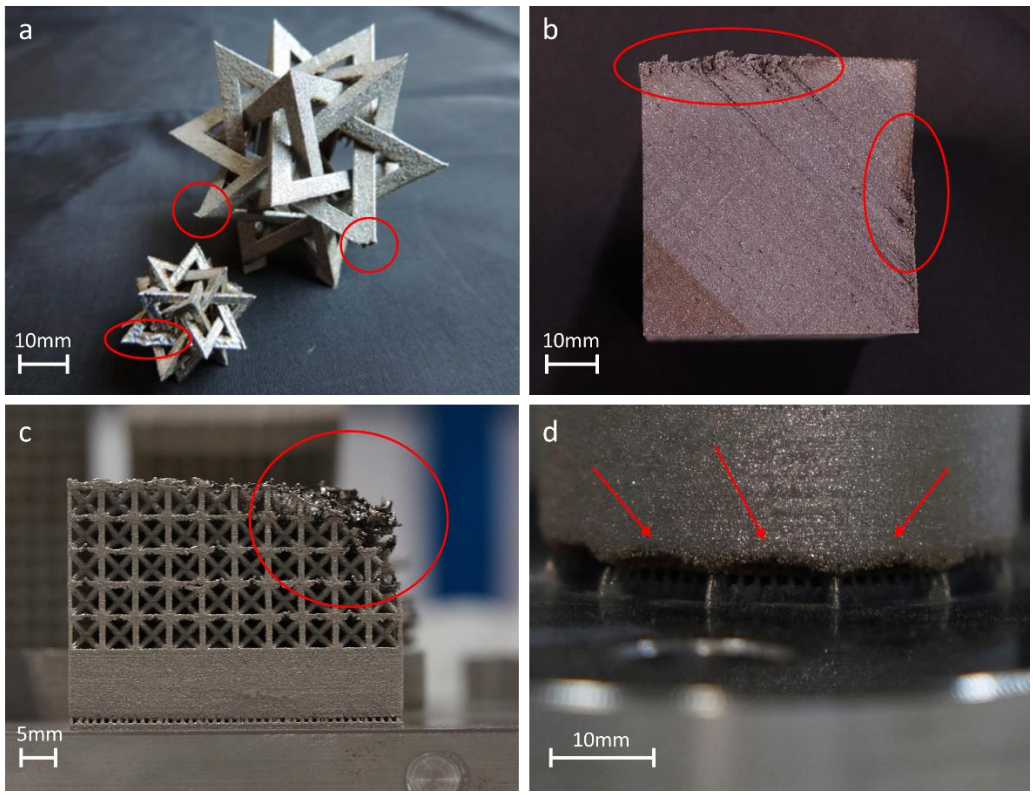


Fig. 1 - Examples of defective parts produced via SLM: local defects in a) complicated geometries, b) contours of solid parts, c) lattice structures, and d) part – support interfaces

Fig. 1 shows four examples of defective parts generated during an SLM process on AISI 316L parts. The defects were either caused by improper heat conduction in overhang features (Fig. 1a and b), a wrong powder deposition due to a worn recoating blade (Fig. 1c) or an improper heat conduction to the underneath powder at the connection between the bottom layers of the part and the supports (Fig. d). All the defects shown in Fig. 1 could have been possibly detected during the process itself, by in-process monitoring. Different authors and research groups have been studying in-process monitoring solutions for SLM systems [11 – 12]. Generally speaking, three different scales can be envisaged to gather data during the process (see Fig. 2).

The first scale involves the characterization of the melt pool and the surrounding heat-affected zone [15 – 17]. The dimensions, shape and temperature distribution of the melt pool provide relevant information about the process stability and the occurrence of local defects. The second scale regards the analysis of the entire layer, to detect errors in different areas of each slice. In this case, different authors focused on the temperature distribution over the slice [18 - 19], on the surface pattern observed at the end of the laser scanning [20] and the reconstruction of the 2D slice geometry [18]. The third scale regards the volumetric growth of the build, from layer to layer. This implies repeating the previous analysis for each layer in order to monitor the overall evolution of the process and its stability along the vertical growth direction.

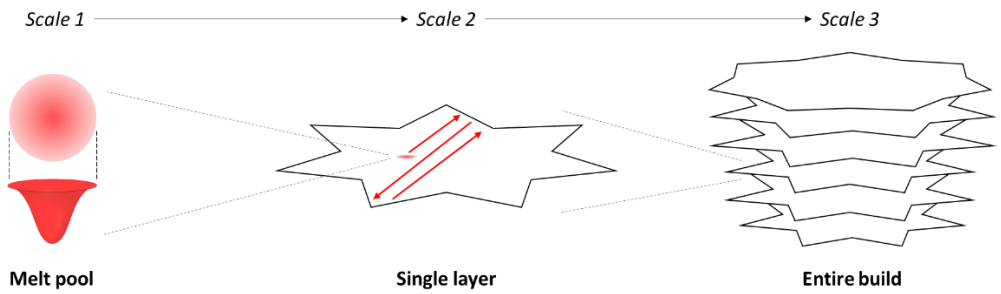


Fig. 2 - Three monitoring scales for SLM processes

This study focuses on the second scale and it aims to detect and spatially localize the onset of process defects via an off-axial machine vision system. The category of defects investigated in this study consists of local overheating phenomena that may cause geometrical distortions. This kind of defect is caused by a wrong heat transfer from the melt pool to the surrounding material that usually occurs in down-facing zones, acute corners and thin walls that are mostly surrounded by loose powder. The major challenge consists of distinguishing between over-heated areas, normal melted zones and spatter tracks. Other phenomena may generate similar “hot spots” during the process, e.g., the deposition of large hot spatters on the powder bed. However, the possible extension of the proposed approach to other defect scenarios will be the subject of a future research.

In the SLM literature, the development of statistical monitoring methodologies and the assessment of suitable control statistics is still in a quite preliminary phase. Abdelrahman and Starr [18] and Schilp et al. [21] discussed a thermography analysis for local overheating detection based on off-axial monitoring. Similarly to the work of Schilp et al. [21], this study proposes a method to estimate a statistical descriptor for the spatial localization of defects associated to overheating phenomena. Contrary to previous

approaches, we propose a statistical method that requires neither process modelling nor image segmentation or edge detection operations. Moreover, differently from previous studies, our proposed quality index is estimated from image streams acquired in the visible range by using an experimental setup that requires no modification of the machine tool configuration, which makes it easily reproducible by practitioners.

The main idea consists of identifying molten areas whose behaviour is different from other portions of the same layer in terms of intensity profiles of each image pixel. To this aim, we propose the use of Principal Component Analysis (PCA) [22] for image data to define a statistical descriptor based on the Hotelling's $T^2$ distance [23 – 24]. An automated method based on k-means clustering [25] applied to the spatial distribution of the $T^2$ distance is then proposed for in-process defect detection. The paper presents a real case study dealing with SLM production of both simple and complicated shapes [26]. The comparison with a basic statistic indicator highlights the benefits of the proposed approach. An analysis to determine the robustness of the methodology to different ways of rearranging the image stream dataset into the PCA input matrix is presented and discussed too.

The paper is organized as follows. Sections 2 describes the case study whereas Section 3 presents the proposed methodology. Section 4 presents the results achieved by applying the proposed approach to the SLM process and eventually Section 5 concludes the paper.

## 2 A REAL CASE STUDY IN SLM

The case study includes both a simple geometry and a complicated shape with critical features produced via SLM. The first one consists of a cylinder, which is representative of an in-control process as no geometrical or surface defects were observed after inspecting and measuring the part. The second one consists of complicated shapes (Fig. 1a - the largest sample)[2], where different defects and geometrical distortions were observed. The SLM was performed on AISI 316L powder by using a Renishaw™ AM250 machine, and both the parts were produced in the same build. Sub-section 2.1 introduces the experimental setup and sub-section 2.2 describes the process parameters, the monitored features and the nature of observed defects.

### 2.1. Experimental Setup

Fig. 3 shows the experimental setup for image stream acquisition that consists of an Olympus™ I-speed 3 camera placed outside the build chamber, which includes a CMOS sensor and operates in the visible range and mounts a SIGMA $105\ mm$ macro lens. The frame rate was selected by finding a compromise between the capability of tracking the laser kinematics without losing relevant information and the computational feasibility of in-process image analysis implementation. To this aim, a sampling frequency of $f = 300\ fps$ was selected, corresponding to a spatial resolution of $1280 \times 1024$ pixels.

[2] The CAD model of this part is available at https://grabcad.com

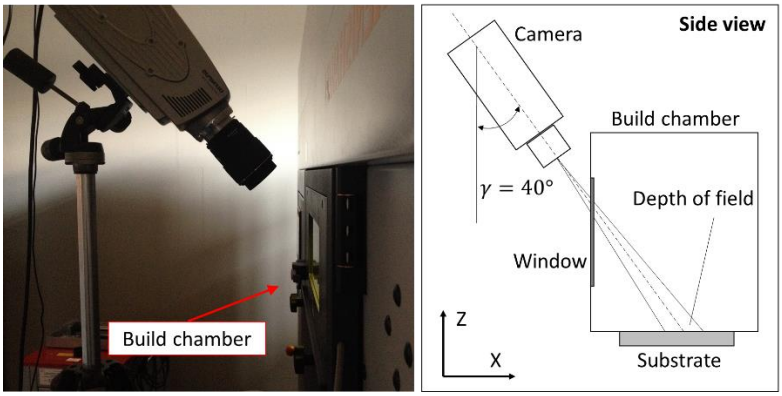


Fig. 3 - Experimental setup with the high-speed camera outside the build chamber: side view picture (left panel) and schematic representation of the same view (central panel)

The experimental setup adopted in this study requires no modification of an existing machine tool configuration and hence it can be easily reproduced by practitioners. Future research will be aimed at extending this study to image stream acquired at different frame rates or by using a different experimental setup. It is worth to notice that by using a camera with a sufficiently high spatial resolution and a proper lens, it is possible to capture the entire layer and hence to detect possible defects in every region of the build. Unfortunately, the high-speed acquisition and processing of high-resolution images that cover such a wide area implies very high computational costs and expensive tools. In this study, the image acquisition setup was aimed at monitoring a limited portion of the entire build area. Possible technological extensions to demonstrate larger area monitoring capabilities may be the subject of future studies.

### 2.2. Process Parameters And Monitored Features

Default laser and scanning parameters suggested by the machine tool manufacturer were considered during SLM. Table 1 shows the main parameters, where power ($P$), exposure time ($t$) and focus position ($f_p$) relate to the laser settings, the point distance, $d_p$, is the distance between the single laser spots along the scan direction, whereas the hatch distance, $d_h$, is the distance between successive scanned hatches when using a meandering scanning path. Eventually, the laser spot is about $70\ \mu m$.

Table 1 - Main process parameters used in the case study

| Parameter | Power ($P$) | Exposure time ($t$) | Focus position ($f_p$) | Point distance ($d_p$) | Hatch distance ($d_h$) |
|---|---|---|---|---|---|
| Value | $200\ W$ | $80\ \mu s$ | $0\ mm$ | $60\ \mu m$ | $110\ \mu m$ |

An AISI 316L powder with average particle size of about $25 - 30\ \mu m$ was used, and the powder layer thickness was set to $50\ \mu m$. The cylindrical part has diameter $\emptyset = 16\ mm$ and height $h = 44\ mm$ and it was built perpendicularly to the supporting platform. The complicated geometry is about $50 \times 50 \times 50\ mm$ and no supports were used apart from the ones underneath the base corners used to ease the part removal from the substrate. This latter part was chosen because it exhibits different criticalities. Indeed, a large portion of part slices includes features with down-facing acute corners, where overheating phenomena and local defects are more likely to occur.

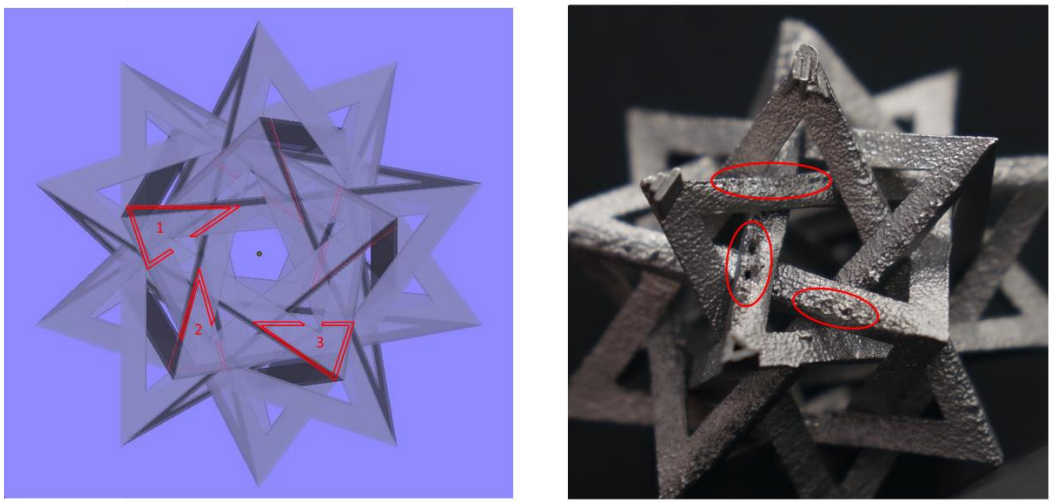


Fig. 4 - Left panel: bottom view of the CAD model, where three triangular features resulting from part slicing are highlighted (referred respectively as triangle 1, 2 and 3); right panel: bottom view of manufactured part showing the effects of local over-heating in overhang acute corners

The image data presented in this study refer, respectively, to one in-control layer of the cylindrical part and a few out-of-control layers in the lower portion of the complicated part. With regard to the out-of-control examples, each slice consists of multiple triangular features. Fig. 4 (left panel) shows a bottom view of the CAD model, where three triangular features resulting from slicing the part are highlighted in red: they will be named “triangle 1”, “triangle 2” and “triangle 3” in the following. The acute corners of triangle 1, 2 and 3 belong to down-facing zones, where the most severe defects were observed. Fig. 4 (right panel) shows a bottom view of the final part, which highlights the defective zones corresponding to these down-facing acute corners.

Fig. 5 shows a larger view of triangle 1, 2 and 3 where the corners are identified by using capital letters. The laser scanning path for triangle 1 and a detail view of corner

C are shown in Fig. 6, in left and right panel, respectively. The scanning path in Fig. 6 includes normal borders and hatches, together with down-facing and up-facing borders and hatches.

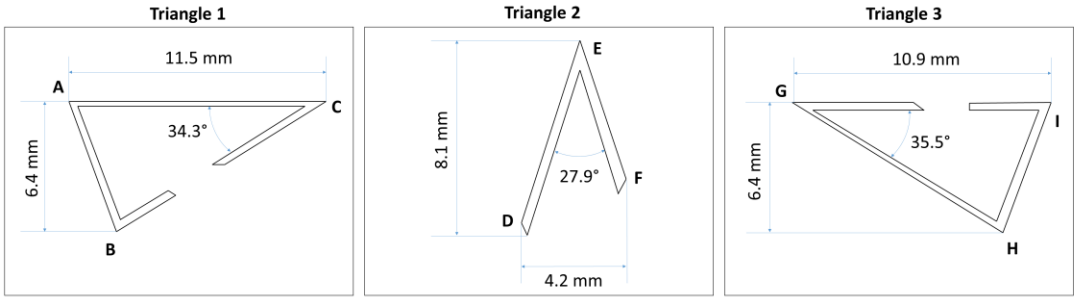


Fig. 5 - Triangular features resulting from slicing the CAD model of the part

The local overheating, caused by a wrong heat transfer toward underneath and surrounding loose powder, yielded defects in corners C, E and G. The major difference between a normal melting zone and an over-heated zone regards the cooling rate. A normal melting zone is characterized by a high cooling rate that leads to a finer grain and stiffer material. Over-heated zones, instead, exhibit quite low cooling rates because of an improper heat transfer to the surrounding material. Indeed, the corners C, E and G exhibited a longer cooling transitory than other parts of the slice. This overheating phenomenon rapidly yielded a super-elevation of the acute corners leading to a growth of defect severity from one layer to another.

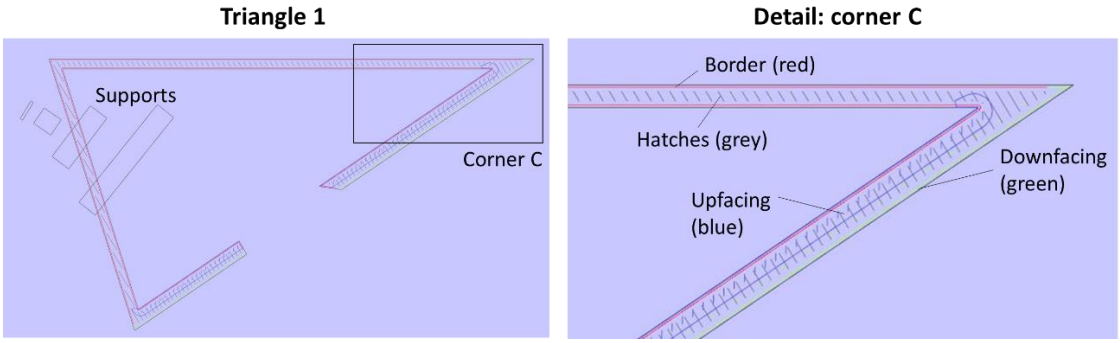


Fig. 6 - Example of laser scanning path for triangle 1 (left panel) and detail of corner C (right panel): borders in red, hatches in grey, up-facing paths in blue and down-facing paths in green (see the on-line version of the paper for color figures)

In this study, the laser scanning of one triangular feature per layer was acquired, such that triangle 1 was the portion of slice monitored in layer 149, triangle 2 was monitored in layer 150 and triangle 3 was monitored in layer 151. The overall number of layers of the build was 1040. This resulted in three distinct image streams associated to different portions of part slices. The methodology presented in Section 3 can be extended to monitor not only the entire slice but also successive layers of the same process.

## 3 METHODOLOGY

The proposed approach is thought to monitor an SLM process by detecting and locating possible defects in each layer. The image stream acquired during the SLM of a single layer can be represented as a 3-dimensional array, $\boldsymbol{\mathcal{U}} \in \mathbb{R}^{J \times M \times N}$, where $J$ is the total number of acquired frames, and $M \times N$ is the size, in pixels, of each frame (see Fig. 7). The 3-dimensional array is such that $\boldsymbol{\mathcal{U}} = \{\boldsymbol{U}_1, \boldsymbol{U}_2, \dots, \boldsymbol{U}_J\}$ where $\boldsymbol{U}_j \in \mathbb{R}^{M \times N}$ is the $j^{th}$

image of size $M \times N$, and $j = 1, \dots, J$. The $(m, n)$-th element of the matrix $\boldsymbol{U}_j$ represents the intensity of that pixel in the corresponding frame, for $m = 1, \dots, M$ and $n = 1, \dots, N$. As an example, for greyscale images at 8 bpp (bit per pixel) the pixel intensity, $u_j(m, n)$, ranges from 0 to 255, where 0 is black and 255 is white. Being $[t_0, t_0 + \Delta t]$ the time interval associated to the image stream $\boldsymbol{\mathcal{U}}$, then $f = J/\Delta t$ is the frame rate of the video.

The $1 \times J$ vector $\boldsymbol{u}(m, n) = \left[u_1(m, n), \dots, u_J(m, n)\right]^T$ represents the intensity profile of the $(m, n)$-th pixel over the $J$ acquired frames. Notice that here the term "intensity profile" is referred to the intensity pattern of a single pixel along the image stream. The underlying idea of the proposed approach consists of studying the variability of all the pixel intensity profiles, and identifying pixels (or groups of pixels) whose profile deviates from the in-control pattern that describes the data structure. To this aim, we propose a PCA-based methodology [22] to characterize the in-control data pattern and to estimate a statistical descriptor based on the Hotelling's $T^2$ distance [24]. A k-means clustering analysis [25] is then used to automate the detection and localization of the defect area.

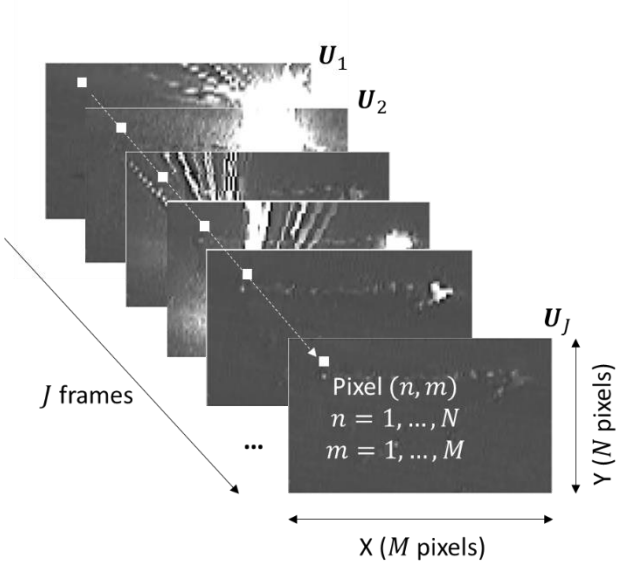


Fig. 7 - Example of an image stream that consists of $J$ frames of size $M \times N$ pixels

The method is first presented as a tool for the spatial identification of local defects at the end of the layer scanning, i.e., when the entire image stream $\boldsymbol{\mathcal{U}} = \{\boldsymbol{U}_1, \boldsymbol{U}_2, \dots, \boldsymbol{U}_J\}$ is available. The method is then extended to provide an iterative update of the statistical descriptor during the scanning of the current layer, in order to anticipate the identification of the defect.

An overview of the two major steps of the proposed approach are presented in sub-section 3.1 and 3.2, whereas its extension via iterative updating is discussed in sub-section 3.3.

### 3.1. Statistical Descriptor Estimation Via PCA

The PCA has been used for image analysis and classification by different authors [22; 27 – 31], also in the frame of manufacturing process monitoring [32 – 34]. A common

way to apply the PCA to image data, a.k.a. vectorised PCA (VPCA), entails the "vectorization" operation, which involves the transformation of bi-dimensional samples (i.e., the frames) into one-dimensional vectors. The result is a transformation from a 3-dimensional array into a matrix that is known as "unfolding" operation. A brief overview of the VPCA methodology is presented in Appendix A.

In the traditional SPC framework, the VPCA is applied to a dataset that consists of random replicates of the same type of image and the goal is to associate a control statistic value to each of them for either monitoring or classification purposes. This implies an unfolding operation like the one shown in Fig. 8, on the left.

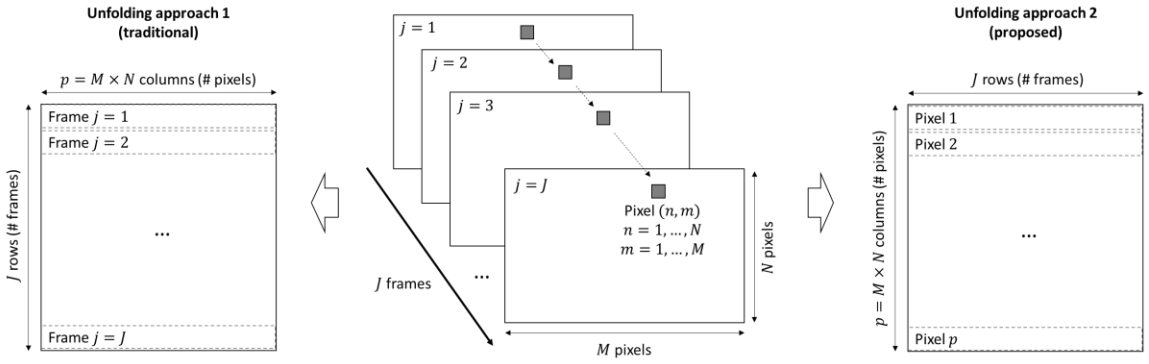


Fig. 8 - Traditional (left) and proposed (right) unfolding approaches from $\mathbb{R}^{J \times M \times N}$ to $\mathbb{R}^{J \times p}$ and to $\mathbb{R}^{p \times J}$, respectively, where $p = M \times N$

Fig. 8, left side, shows a transformation from the 3-dimensional array $\boldsymbol{\mathcal{U}} \in \mathbb{R}^{J \times M \times N}$ to a matrix $\mathbf{X} \in \mathbb{R}^{J \times p}$, where $p = M \times N$. Each row of the matrix consists of a vectorised frame. The VPCA generates PCs that associate a weight to each pixel. A statistical descriptor based on the Hotelling's $T^2$ distance [24] associates a value to each

frame, such that the larger is the $T^2$ value, the more outlying is the corresponding frame pattern from the underlying image data structure [32 – 34].

The image stream dataset used in this study exhibits two major differences from the aforementioned framework. The first difference consists of the fact that the video frames are not replicates of a single image, but they capture successive stages of the SLM process. Second, the goal is not to signal an anomalous frame, but to identify a portion of the images (i.e., a group of pixels) characterized by an anomalous pattern. Because of this, a different implementation of the PCA technique is presented. It involves performing the unfolding operation as shown in Fig. 8, on the right.

In this case, the 3-dimensional array $\boldsymbol{\mathcal{U}} \in \mathbb{R}^{J \times M \times N}$ is transformed into a matrix $\mathbf{X} \in \mathbb{R}^{p \times J}$, where $p = M \times N$. Each row of the matrix consists of a pixel intensity profile, i.e., the $1 \times J$ vector $\boldsymbol{u}(m,n) = \left[u_1(m,n), \dots, u_J(m,n)\right]^T$. The VPCA generates PCs that associate a weight to each frame. Thus, each PC is a $1 \times J$ vector that weights each time-location of pixel intensity profiles. This unfolding strategy is analogous to the so called "T-mode PCA" used in multidimensional data analysis [22].

The statistical descriptor based on the Hotelling's $T^2$ distance is a spatial index, i.e., a function $T^2(X,Y)$ of pixel location within the image, which maps a $T^2$ value to each pixel. The more outlying is the pattern of a pixel with respect to the underlying pattern captured by the VPCA, the largest is the corresponding $T^2(X,Y)$ value. This yields a spatial localization of the possible defect in a complete data-driven way, without any ad-hoc pre-processing step.

It is evident that there are many ways to arrange the pixel intensity vectors, $\boldsymbol{u}(m,n)$, into the rows of $\mathbf{X}$, e.g., row-wise, column-wise or randomized ordering. Since the variance-covariance structure of the transformed dataset may depend on the pixel arrangement in the $\mathbf{X}$ matrix, it is important to assess the robustness of the proposed approach against such arrangements. In the following, a row-wise arrangement is used as a baseline solution, whereas the robustness of the method is investigated in Section 4, by comparing different approaches.

### 3.2. K-Means Clustering For Automated Defect Detection

Once the $T^2(X,Y)$ descriptor has been estimated (see Appendix A), an automated procedure is required to signal the presence of an area of the images where pixel intensity profiles exhibit an unnatural pattern. In this study, we propose a method based on k-means clustering analysis. The k-means algorithm represents an effective and popular clustering technique that allows partitioning $p$ observations into $k \leq p$ clusters to minimize the within-cluster sum of squared distances from the cluster centroid [25]. When the k-means approach is applied to image or surface data it provides a segmentation into $k$ areas characterized by maximum within similarity [35]. In this study, the k-means methodology is not applied to the original images but to the spatial distribution of the $T^2(X,Y)$ descriptor. A predefined number, $k$, of centroids is randomly placed in the $M \times N$ image space and the image pixels are then associated to the closest centroid in terms of Euclidean distance between $T^2(X,Y)$ values. The process is repeated iteratively until the centroids stabilize about a fixed position in the image space.

Hierarchical clustering [23, 25] represents an alternative way to achieve a similar segmentation but, generally speaking, it is less computationally efficient and it suffers from combinatorial explosion as the number of pixels grows [25, 35]. Thus, the k-means approach is applied in this study, but future research developments may investigate the effectiveness of different clustering techniques.

In the absence of local defects, two distinct regions must be present: one corresponding to the background, involving lower values of $T^2(X,Y)$, and one corresponding to the trace of both heated zone and spatters in the visible range. In normal process conditions, the $T^2(X,Y)$ distribution should be partitioned into these two regions. In the presence of a defect caused by a local overheating, a third region is expected to appear, corresponding to a local peak of $T^2(X,Y)$. Our proposed approach consists of clustering the $T^2(X,Y)$ spatial distribution into a data-driven selected number $k$ of clusters. As soon as $k > 2$ clusters are detected, i.e., when at least one extra cluster is generated, an alarm can be signalled.

The data-driven choice of the "correct" number of clusters is known as "*cluster validity*" problem [36]. Many different criteria have been proposed so far. A wide category of validity criteria relies on the measure of the within-group variance and the between-group variance [36 – 40]. A method that provides satisfactory results in a wide range of applications consists of looking for an elbow point in the sums of squared within-distances (SSWs) between the $T^2$ value of each pixel and the mean value of the corresponding cluster, for different numbers $k$. The $SSW(k)$ index can be computed as follows:

$$SSW(k) = (1/k)\sum_{k=1}^{K}\sum_{i\in c_k}\left\|T_i^2(X,Y)_{c_k} - \overline{T^2}(X,Y)_{c_k}\right\|,\ k = 1,2,\dots,K \quad (1)$$

where $T_i^2(X,Y)_{c_k}$ is the $T^2$ value of the i-th pixel belonging to the $c_k$ cluster, $\overline{T^2}(X,Y)_{c_k}$ is the mean $T^2$ value of the corresponding cluster, and $K \leq p$ is the maximum number of tested clusters, to be selected ex-ante. $SSW(k)$ is a monotone decreasing function of the number of clusters $k$, which is normalized with respect to the number of clusters to reduce the risk for over-segmentation.

A common way to find the elbow point consists of computing the distance, $D(k)$, between $SSW(k)$ and the straight segment connecting the two extreme points, $SSW(1)$ and $SSW(K)$. The elbow of the function, i.e., the number of clusters $k$ that provides the best partition of the $T^2(X,Y)$ spatial distribution, is $\hat{k} = \underset{k}{\operatorname{argmax}}\, D(k)$.

This procedure for cluster validation is suitable when the minimum number of clusters is $k = 2$, which is the case of the present application, where the natural spatial distribution of $T^2(X,Y)$ consists of two clusters, and the appearance of additional clusters is a symptom for local defect generation.

### 3.3. A Within-Layer Extension Of The Proposed Approach

The method presented in the previous sections allows one to estimate and analyze the spatial indicator at the end of the layer scanning, as it requires the acquisition of all the $J$ frames of the image stream, $\boldsymbol{\mathcal{U}} \in \mathbb{R}^{J\times M\times N}$. Nevertheless, it is possible to extend the methodology in order to achieve a faster detection of possible defects via an iterative

updating of the VPCA model estimation. To this aim, the method can be extended as follows. Let $\boldsymbol{\mathcal{U}}_1 \in \mathbb{R}^{J' \times M \times N}$ be a first batch of $J'$ frames such that $1 < J' \leq J$ and let $\mathbf{X}_1$ be its unfolded version. By applying the VPCA to the matrix $\mathbf{X}_1$ it is possible to study the variance-covariance structure of the pixel intensity profiles from frame $j = 1$ up to frame $j = J'$. If an anomalous pattern is present within the first $J'$ frames, the k-means clustering approach based on the $T_1^2(X, Y)$ indicator will aid its detection, where the subscript "1" refers to the use of $\mathbf{X}_1$ matrix. The estimation of the VPCA model can be updated when a new batch of $J'$ frames is available, such that $2J' \leq J$. The spatial descriptor can be updated as well, leading to a new spatial distribution, $T_2^2(X, Y)$, and an updating of the clustering analysis. The former step can be iteratively repeated until the laser scanning of the current layer is over.

## 4 DISCUSSION OF RESULTS

The results achieved by applying the proposed approach at the end of the layer scanning are first discussed in sub-section 4.1. The results achieved by applying the iterative updating extension of the method are presented in sub-section 4.2, and a comparison against a competitor approach based on the mean pixel intensities is discussed in sub-section 4.3. Eventually, sub-section 4.4 presents a robustness analysis with respect to the ordering of image pixels in the VPCA input matrix.

### 4.1. Entire Image Stream Analysis

#### *4.1.1. In-control process monitoring*

In this subsection, the results achieved by monitoring one in-control layer of the cylindrical part are discussed. The total number of acquired frames is 400 and the image size after a crop operation is $310 \times 220$. Image cropping can be automatically set before starting the image acquisition, since the size of the monitored feature/slice is known.

Fig. 9 (right panel) shows the spatial distribution of the $T^2(X,Y)$ descriptors when the VPCA is applied to the entire image stream of the monitored slice. The $T^2(X,Y)$ indicator is based on the minimum number of PCs that explains at least 80% of the overall image data variability (see Appendix A for details). In this case, the number of retained PCs is $m = 10$. The $T^2(X,Y)$ descriptor exhibits the largest values over the scanned area of the slice but its spatial distribution also shows the track of hot spatters generated during the process (upper part of the scanned area). Fig. 9 (central panel) shows the results of the k-means clustering applied to the circular slice. The automatic selection of cluster numbers yields $k = 2$ in all the considered cases (see the $D(k)$ statistics in the left panel of Fig. 9). One cluster (represented by the black area) corresponds to the background region. The second cluster (represented by the grey area) corresponds to the normal melting zone.

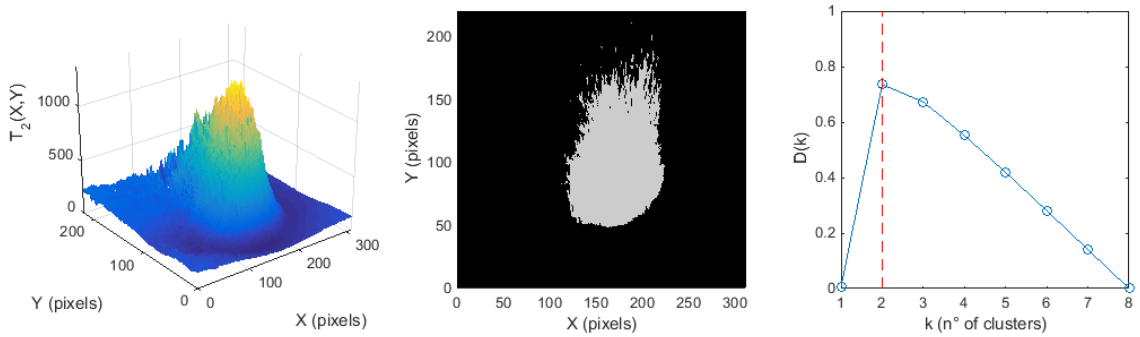


Fig. 9 - Spatial distribution of $T^2(X,Y)$ for one slice of the cylindrical shape (left panel); clusters identified using the k-means approach (central panel; black: background, grey: normal melting) and corresponding $D(k)$ statistics (right panel)

These two clusters are expected to represent the natural (in-control) state of the process, as discussed in the previous section. The lack of further clusters is representative of the lack of local defects characterized by anomalous melting conditions.

### *4.1.2. Out-of-control process monitoring*

In this subsection, the results achieved by monitoring the defective part are discussed. The total number of frames acquired for each monitored feature, i.e., triangles 1, 2 and 3, together with the corresponding image sizes after a crop operation are listed in Table 2. With regard to the computational feasibility of the VPCA-based approach, the analysis of a $8591 \times 350$ matrix that results from the unfolding of 350 frames of size $121 \times 71$ required about $0.15\ s$ on a laptop equipped with an Intel® Core™ i7-3537 CPU @ 2.00 GHz. Although this makes the method suitable for in-process monitoring via batch analysis, future research efforts may be devoted to investigate more efficient PCA variants and algorithm implementations.

Table 2 - Number of frames and image sizes for different monitored features

| Monitored feature | Total number of frames ($J$) | Image size (pixels) |
|---|---|---|
| Triangle 1 | 350 | $121 \times 71$ |
| Triangle 2 | 200 | $121 \times 71$ |
| Triangle 3 | 350 | $121 \times 71$ |

An example of the pixel intensity profiles, $\boldsymbol{u}(m,n) = \left[u_1(m,n), \ldots, u_J(m,n)\right]^T$, for three pixels belonging, respectively, to the three corners, A, B and C, of triangle 1, are shown in Fig. 10. The pixel intensity ranges between 0 (black) and 255 (white), whereas the background intensity is about 80.

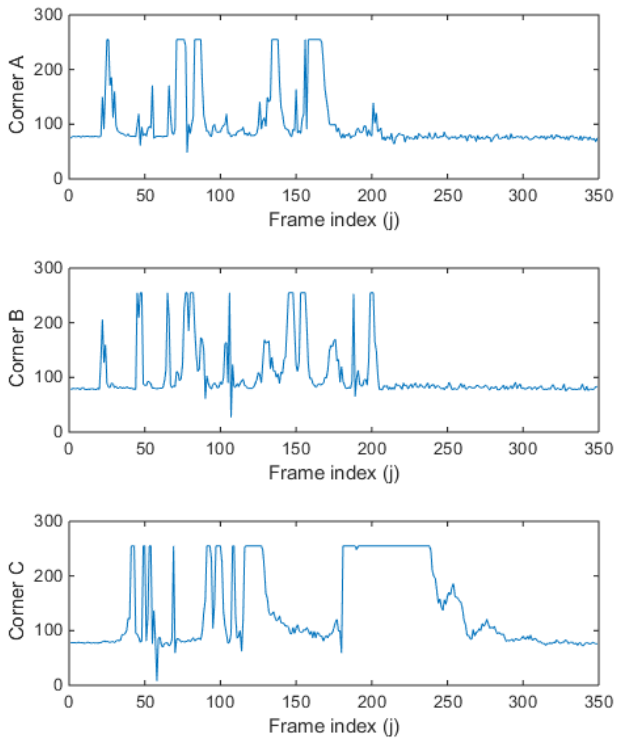


Fig. 10 - Examples of three intensity profiles for pixels belonging to corner A (top panel), corner B (central panel) and corner C (bottom panel) – triangle 1

The intensity profiles of pixels in corner A and B (Fig. 10, top and central panels) are representative of a normal melting. The intensity peaks correspond to frames where either the high intensity area surrounding the laser spot or one (or more) spatters passed over the corresponding pixel. Due to the scanning strategy that involves internal hatches and borders, a single pixel is scanned more than once during the SLM phase. The intensity profile of pixels belonging to corner C (Fig. 10, bottom panel) is representative of a defective melting, due to a local overheating. Such an overheating causes a slow cooling transitory after the intensity peak at about frame $j = 125$ and, more evidently, the long lasting pixel saturation that starts at about $j = 180$. The pixel intensity decreases very slowly and it reaches the background intensity only after the SLM of the feature is over.

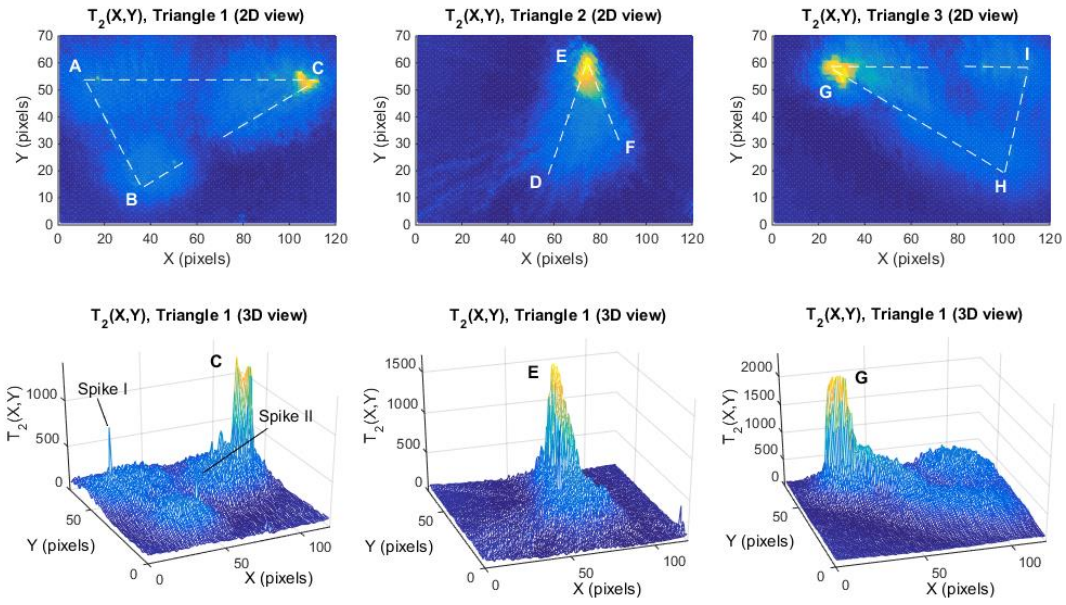


Fig. 11 - 2D (top panels) and 3D (bottom panels) representations of the spatial distribution of $T^2(X,Y)$ for triangle 1 (left panels), triangle 2 (central panels) and triangle 3 (right panels); the colour map ranges from dark blue (lower values) to bright yellow (larger values) (see the on-line version of the paper for color figures)

Fig. 11 shows the spatial distribution of the $T^2(X,Y)$ descriptors when the VPCA is applied to the entire image stream of each monitored feature. Fig. 11 (top panels) shows a 2D representation of the $T^2(X,Y)$ descriptors, where the centre line of each triangle (dashed white line) is superimposed. Fig. 11 (bottom panels) shows the 3D views of the same statistic. The $T^2(X,Y)$ indicator is based on the minimum number of PCs that explains at least 80% of the overall image data variability (see Appendix A for details). In this case, the number of retained PCs is respectively $m = 12$, $m = 10$ and $m = 10$ for triangle 1, triangle 2 and triangle 3. A discussion about the physical meaning of the resulting PCs and the related statistics is presented in Appendix B.

Fig. 11 shows a peak of the $T^2(X,Y)$ descriptor corresponding to corners C, E and G, i.e., the down-facing acute corners where the overheating phenomenon occurred. Such a high value is due to the fact that pixels in those zones are characterized by an intensity profile that is considerably different from the underlying pattern that describes the image stream (see Fig. 10). This makes the VPCA-based $T^2(X,Y)$ descriptor a suitable spatial index for in-process detection of local defects associated to overheating problems. Fig. 11 also shows that some single-point spikes are present. In particular, Fig. 11 (bottom-left panel) highlights two spikes in the spatial distribution of $T^2(X,Y)$ for triangle 1, called spike I and II. The two intensity profiles corresponding to these spikes are shown in Fig. 12. These two pixels exhibit an anomalous pattern in the last frames: their intensity does not go down to the background value, but it fluctuates around higher values. This may be

caused by a local reflection of light towards the lens, a deposition of a hot spatter, or something else that deserves a further investigation.

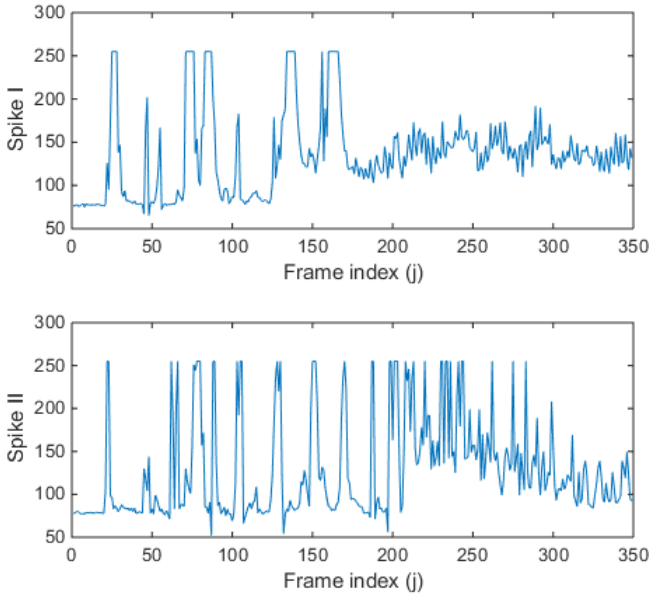


Fig. 12 - Example of intensity profiles corresponding to pixels that exhibit a spike of the $T^2(X,Y)$ indicator identified as spike I and spike II (triangle 1)

Fig. 13 (top panels) shows the results of the k-means clustering applied to the three triangular features. The automatic selection of cluster numbers yields $k = 3$ in all the considered cases (see the $D(k)$ statistics in the bottom panels of Fig. 13). One cluster (represented by the black area) corresponds to the background region. A second cluster (represented by the grey area) corresponds to the normal melting zone. The third cluster (represented by the red area[3]) corresponds to the peak of $T^2(X,Y)$ values[4].

[3] See the on-line version of the paper for color figures.
[4] In all the considered cases, the k-means algorithm was implemented by setting one hundred iterations, each one corresponding to a randomly generated starting position of cluster centroids

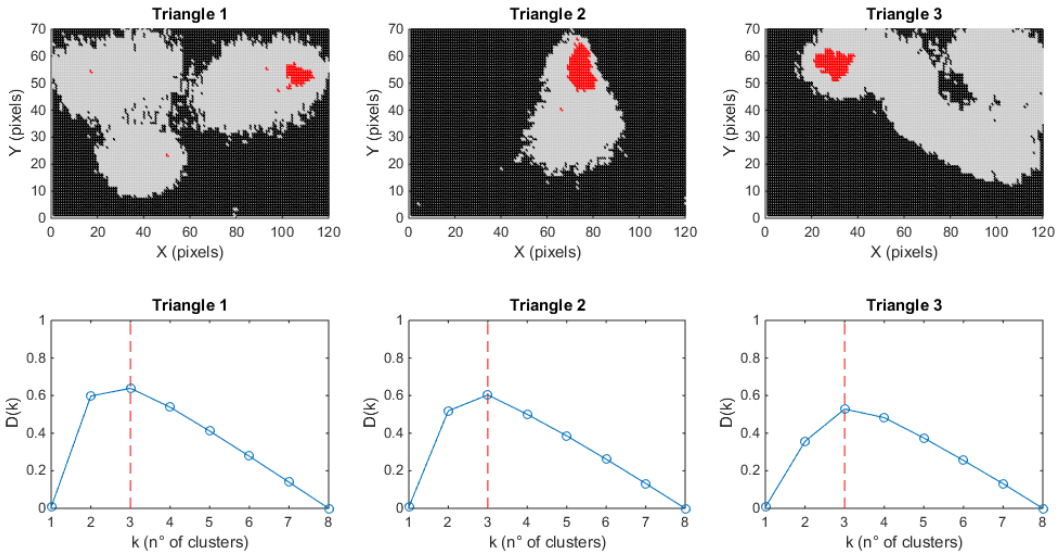


Fig. 13 - Clusters identified using the k-means approach in the out-of-control examples (top panels; black: background cluster, grey: normal melting cluster, red: defect cluster) and corresponding $D(k)$ statistics (bottom panels; vertical red dashed line corresponds to the selected number $k$ of clusters); see the on-line version of the paper for color figures

The first two clusters are expected to represent the natural state of the process, whereas the presence of the third cluster is a symptom of a non-homogeneous heating condition due to the onset of a local defect. Fig. 13 shows that the proposed approach is able to signal also the two major spikes in the image stream associated to triangle 1, i.e., spike I and II, and one large spike in the image stream associated to triangle 2. The knowledge of spatial localization of these spikes is relevant from an in-process monitoring perspective, as they can represent local anomalies that may produce defect onsets in the next layers.

## 4.2. Within-Layer Monitoring Results

### *4.2.1. In-control process monitoring*

In order to show the potential benefits of the within-layer monitoring procedure, the iterative updating of the proposed approach was first applied to the in-control example. We decided to split the duration of the process into $n = 8$ batches, such that $J' = 50$ for triangle 1 and 3 (corresponding to about $0.165\ s$). This means that the estimate of the VPCA-based indicator and the k-means results are updated every $J'$ frames. The choice of the batch size, $J'$, depends on different factors. On the one hand, a sufficient number of frames is required to initialize the VPCA–based estimation. On the other hand, a smaller batch size may provide a faster detection of defects. The computational effort for VPCA updating should be taken into account as well.

Fig. 14 shows the result of the k-means clustering iteratively updated for an increasing number of frames during the laser scanning of the cylindrical shape. Only the two natural clusters (black and grey areas in the figure) are always present, although their separation evolves during the SLM process. The lack of any further cluster in all the recursively updated time windows is representative of a process that is stable over time.

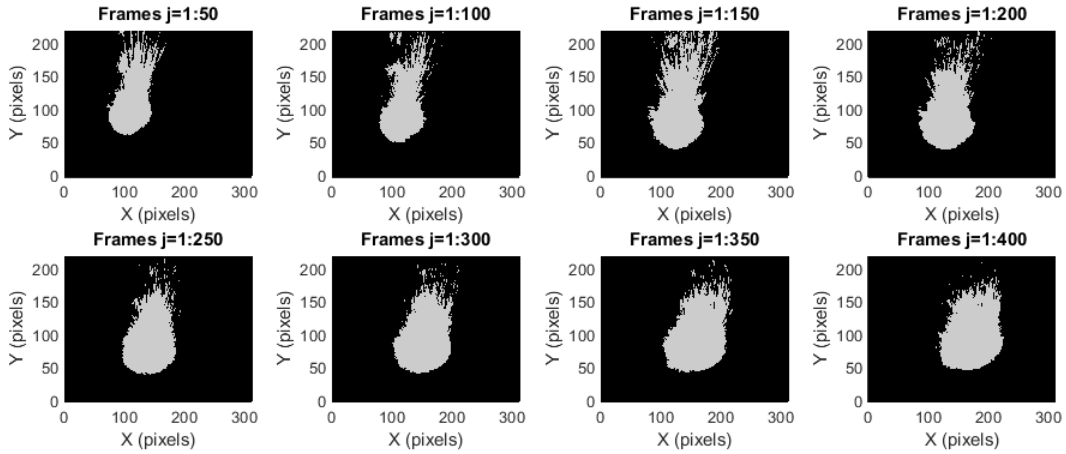


Fig. 14 - k-means clustering of the $T^2(X,Y)$ statistic iteratively updated for a growing number of frames for one slice of the cylindrical shape (black: background, grey: normal melting)

### *4.2.2. Out-of-control process monitoring*

The iterative updating of the proposed approach was applied to the out-of-control examples. Analogously to the in-control case, we split the duration of the process into $n = 8$ batches, such that $J' = 45$ for triangle 1 and 3 (corresponding to about $0.15\ s$), and $J' = 25$ for triangle 2 (corresponding to about $0.08\ s$).

Fig. 15 shows the result of the k-means clustering iteratively updated for an increasing number of frames during the laser scanning of triangle 1. Fig. 15 shows that the two natural clusters (black and grey areas in the figure) are always present, although their separation evolves during the SLM process. A third cluster (red area[5]) starts to be signalled starting from the fifth batch, corresponding to the $T^2(X,Y)$ peak in corner C.

[5] See the on-line version of the paper for color figures.

This means that a recursive update of the proposed approach allows a faster detection of a possible defect, even before the SLM of a complete slice is over.

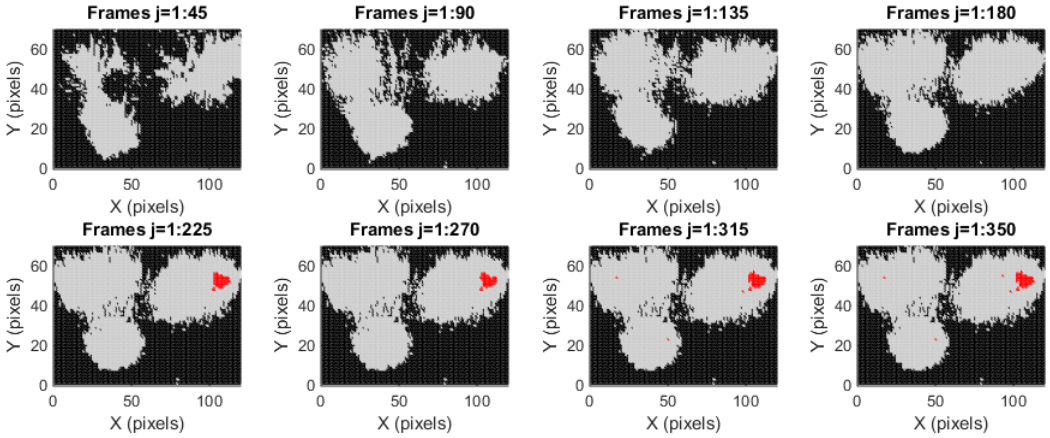


Fig. 15 - k-means clustering of the $T^2(X,Y)$ statistic iteratively updated for a growing number of frames for triangle 1 (black: background, grey: normal melting, red: defect); see the on-line version of the paper for color figures

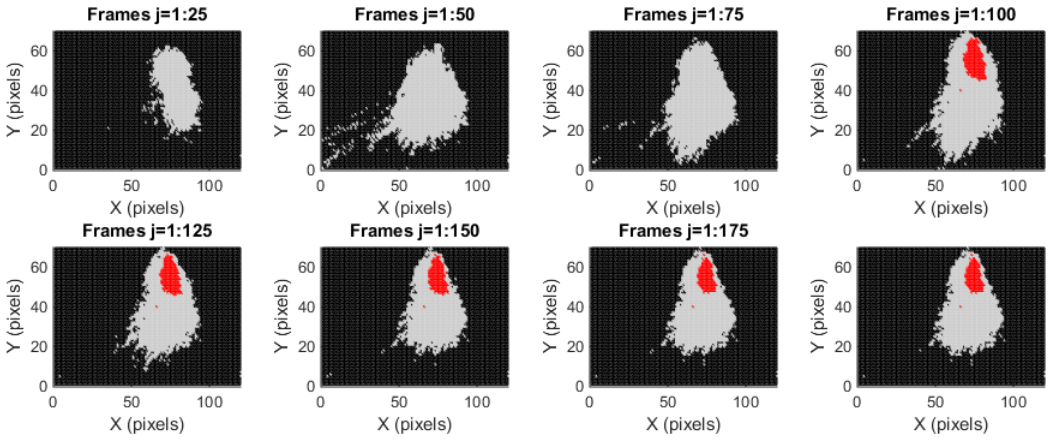


Fig. 16 - k-means clustering of the $T^2(X,Y)$ statistic iteratively updated for a growing number of frames for triangle 2 (black: background, grey: normal melting, red: defect); see the on-line version of the paper for color figures

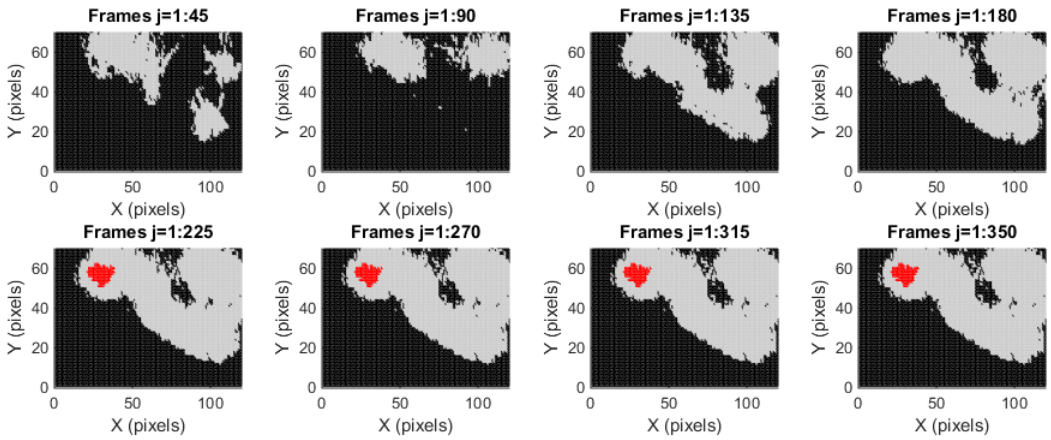


Fig. 17 - k-means clustering of the $T^2(X,Y)$ statistic iteratively updated for a growing number of frames for triangle 3 (black: background, grey: normal melting, red: defect); see the on-line version of the paper for color figures

In case of triangle 2, Fig. 16 shows that the local defect starts to be clearly visible and distinct from other clusters at the fourth batch. In case of triangle 3, Fig. 17 shows that the local defect starts to be signalled at the fifth batch.

### 4.3. A Comparison Study

Due to the emerging nature of the research problem, there are neither actual benchmark approaches nor consolidated techniques to compare with. Nevertheless, it is possible to investigate the benefits of the proposed approach against the use of a simpler statistical descriptor, i.e., the mean intensity of each pixel. The overheating phenomenon yields a local increase of mean pixel intensities in the presence of a defect. Thus, the mean intensity $\overline{\boldsymbol{u}}(m,n) = (1/J)\sum_{j=1}^{J} u_j(m,n)$ might be considered as a reasonable competitor of the $T^2(X,Y)$ descriptor proposed in this study. The k-means methodology was applied

to the spatial distribution of the mean intensity descriptor, and the results are presented in the following.

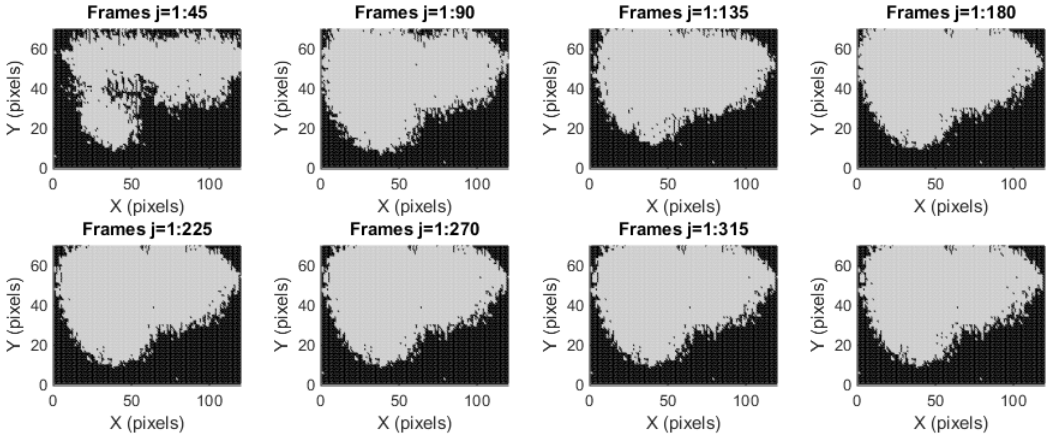


Fig. 18 - Results of competitor approach based on average pixel intensities for triangle 1 (black: background, grey: normal melting, red: defect); see the on-line version of the paper for color figures

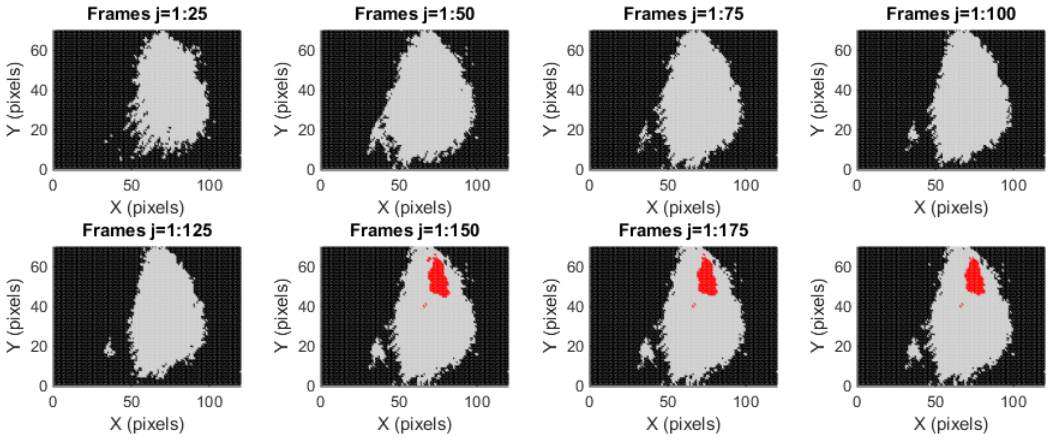


Fig. 19 - Results of competitor approach based on average pixel intensities for triangle 2 (black: background, grey: normal melting, red: defect); see the on-line version of the paper for color figures

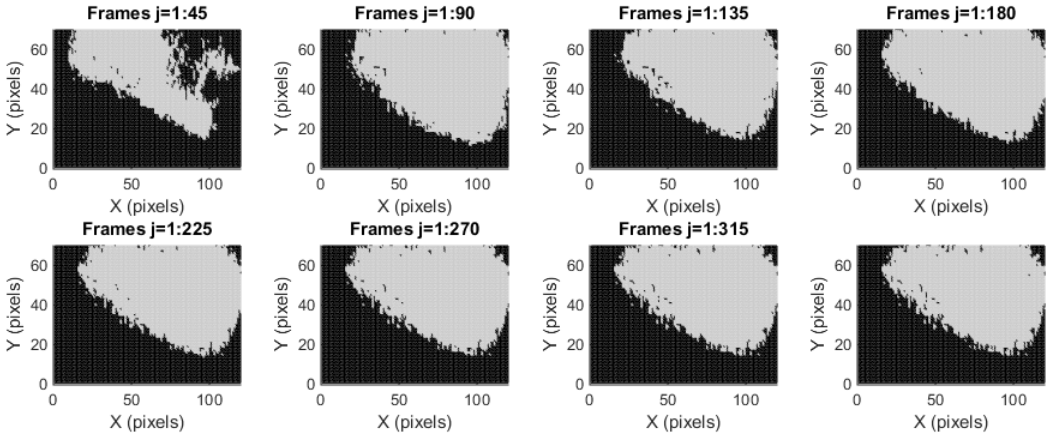


Fig. 20 - Results of competitor approach based on average pixel intensities for triangle 3 (black: background, grey: normal melting, red: defect); see the on-line version of the paper for color figures

Fig. 18 to Fig. 20 show the mean intensity-based clustering results for triangle 1, 2 and 3, respectively. Fig. 18 and Fig. 20 show that, contrary to the proposed approach, the use of the mean intensity descriptor does not allow detecting a third cluster corresponding to the overheated acute corner. This is because there is a smooth and reduced variation of mean intensity between the acute corner and the surrounding area, which prevents the clustering algorithm from identifying two distinct areas.

Fig. 19 shows that, in case of triangle 2, the mean intensity descriptor allows signalling the defect, but the detection occurs later (i.e., at the sixth batch) than in our proposed approach (see Fig. 15). In this case, the gap between the mean intensity of pixels belonging to corner E and the surrounding pixels is sufficiently large to aid a detection of a third cluster, but the $T^2(X,Y)$ descriptor is still preferable. Indeed, the VPCA analysis emphasizes the differences between pixels by taking into account a richer information

than the simple average intensity levels, and this leads to a faster detection of the defect onset.

### 4.4. Robustness To Different Pixel Ordering Strategies

As mentioned in Section 2, the variance-covariance structure of the data matrix $\mathbf{X}$ may be influenced by the approach used to rearrange the $M \times N$ pixels into the $p$ rows of $\mathbf{X}$. The results discussed in sub-section 4.1 and 4.2 were based on a row-wise arrangement, but many other ways for pixel ordering are possible. In order to evaluate the robustness of the $T^2(X,Y)$ spatial distribution against the pixel ordering, four pixel arrangement methods were considered: (1) row-wise arrangement, (2) column-wise arrangement, (3) row-wise arrangement where the within-row order of the pixel was randomized (same ordering for each row), and (4) complete randomization of the pixel order. Fig. 21 shows that the resulting $T^2(X,Y)$ spatial distribution is weakly affected by the pixel order arrangement (as an example, the spatial distribution for triangle 1 is shown). The first and third solutions are basically identical, whereas the second and the forth solution slightly change the distribution of the statistic at lower values and they yield a scale change.

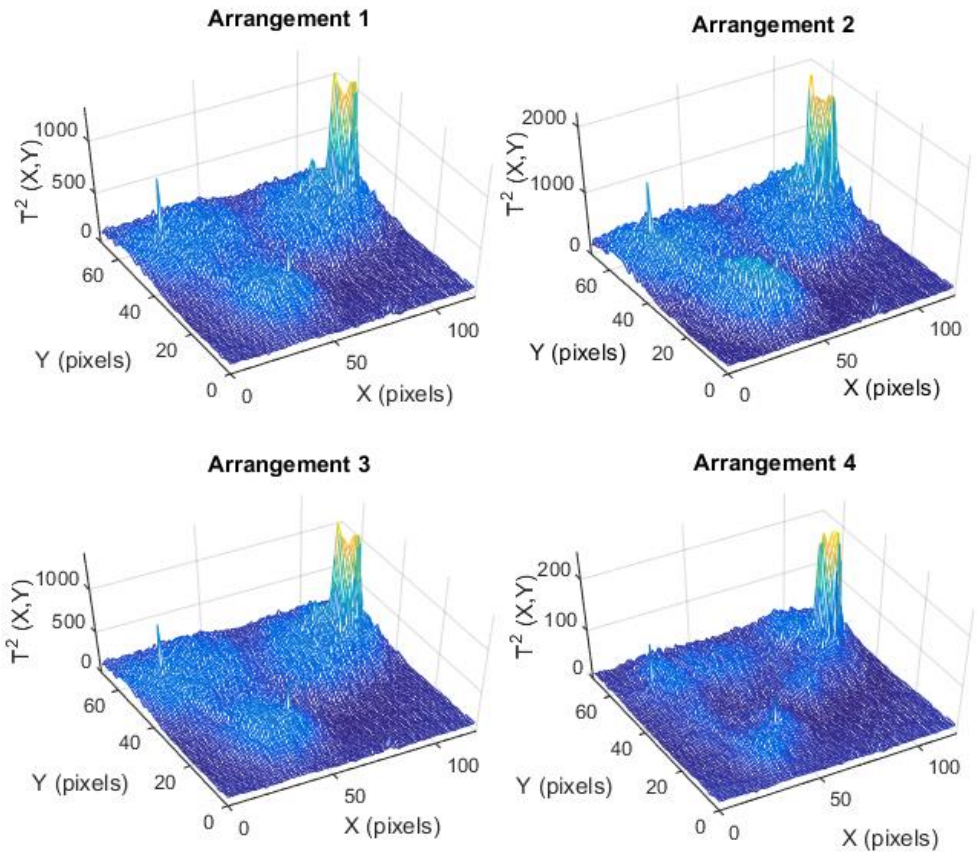


Fig. 21 - $T^2(X,Y)$ spatial distribution for different pixel arranging methods: row-wise (top-left panel) and column-wise (top-right panel), row-wise arrangement with randomized order within the row (bottom-left panel) and complete order randomization (bottom-right panel) – triangle 1

Instead of considering just one possible random ordering, it is possible to estimate the $T^2(X,Y)$ indicator for a larger number of random order realizations and plot the resulting ensemble mean spatial distribution. The mean $T^2(X,Y)$ spatial distribution and the corresponding standard deviation for an ensemble of one thousand realizations are shown in Fig. 22. A standardization was applied in order to estimate the $T^2(X,Y)$ values on the same scale in each realization.

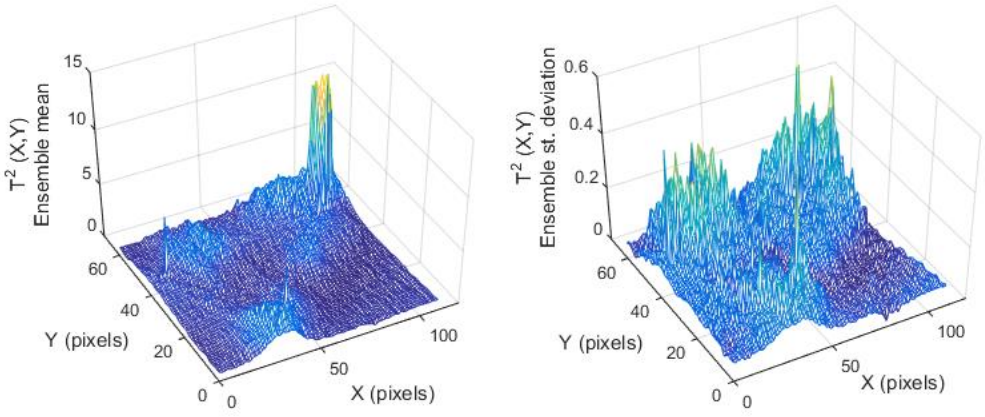


Fig. 22 - Mean $T^2(X,Y)$ spatial distribution (left panel) and the corresponding standard deviation (right panel) for an ensemble of one thousand realizations – triangle 1

The ensemble mean distribution (Fig. 22, left panel) is very close to the distributions shown in Fig, 21, which confirms the robustness of the spatial descriptor against the pixel ordering during the unfolding operation. An ensemble analysis is not computationally suitable for an in-process implementation, and hence the pixel ordering strategy should be selected in advance, but it is expected to have a quite limited impact on process monitoring performances.

## 5 CONCLUSIONS

Despite of the great potential of SLM technologies in many application fields, the process capability still deserves considerable improvements to achieve an industrial breakthrough. Different kinds of defects may originate during the scanning of one single slice and then propagate to the following layers, with a detrimental impact on the geometrical or mechanical/physical properties of the part. In many cases, the defects

affect the internal structure or structural features that are difficult to measure. Thus, they might be hardly visible or detectable by inspecting the final part, but they strongly influence its functionality. Because of this, in-process monitoring plays a relevant role in the development and enhancement of SLM processes, thanks to the capability of detecting the defect onset during the layer-by-layer process itself. Although available SLM systems still lack adaptive/reactive control strategies that can be used for defect mitigation or removal, in-process monitoring has been pointed out as a key enabling technology to pave the way to next generation metal additive manufacturing systems. To this aim, consistent research and development efforts are needed to include in-process monitoring tools into feedback process control loops, possibly by exploiting hybrid manufacturing paradigms.

This paper proposes a method for in-process monitoring of SLM processes via image analysis, which allows both the detection and the spatial localization of local defects related with overheating phenomena. The category of defects investigated in this study consists of local overheating phenomena caused by a wrong heat transfer from the melt pool to the surrounding material.

The proposed approach consists of identifying molten areas whose behaviour is different from other portions of the same layer in terms of pixel intensity patterns over time. An image stream from an off-axial camera was processed via a multi-dimensional version of the PCA, called vectorised PCA. This allows estimating a spatial version of the traditional Hotelling's $T^2$ statistic, which maps a $T^2$ value to each image pixel. A k-means clustering with data-driven selection of the number of clusters, $k$, was then applied to the

spatial descriptor. The results showed that the method is suitable to automatically detect and localize a defect during the layer-by-layer SLM process. A comparison with a simpler statistical descriptor highlighted the effectiveness of the PCA-based methodology. The robustness analysis showed that the spatial descriptor is robust against the strategy used to rearrange the pixel order during the unfolding operation.

The presented case study regarded the SLM of a complicated shape where geometrical and surface finishing defects occurred due to a local overheating in down-facing acute corners of scanned slices. The analysis showed that the proposed approach allows identifying the zones of the slice that exhibit an anomalous cooling transitory resulting from an undesired overheating. Other phenomena may generate “hot spots” similar to the ones corresponding to over-heated zones, e.g., the deposition of large hot spatters on the powder bed. However, the possible extension of the proposed approach to other defect scenarios will be the subject of a future research.

The proposed approach requires no ad-hoc image segmentation or image thresholding operations, and it exploits an experimental setup that implies no modification of the machine configuration. Future developments will be aimed at verifying the suitability and the performances of the proposed approach for image streams acquired with a different frame rate or by using a different experimental setup.

## NOMENCLATURE

| | |
|---|---|
| AM | Additive manufacturing |
| $c_k$ | k-th cluster |
| CMOS | Complementary metal-oxide semiconductor |
| $D(k)$ | Statistic used to select the number of clusters, $k$ |
| $d_h$ | Hatch distance |
| $d_p$ | Point distance between single laser spots |
| $f$ | Video frame rate |
| $f_p$ | Laser focus position |
| $fps$ | Frames per second |
| $J', J$ | Number of frames |
| $k$ | Number of clusters |
| $K$ | Maximum number of clusters |
| $\mathbf{L}$ | Eigenvalue matrix |
| $m$ | Number of retained PC |
| $M \times N$ | Image size in pixels |
| $p$ | Number of pixels |
| $P$ | Laser power |
| PC | Principal component |
| PCA | Principal component analysis |
| $\mathbf{S}$ | Variance-covariance matrix |
| SLM | Selective laser melting |
| SPE | Squared prediction error |
| $SSW(k)$ | Sum of within sum of squared as a function of the number of clusters, $k$ |
| $t$ | Laser exposure time |
| $T^2$ | Hotelling's statistic |
| $\boldsymbol{\mathcal{U}}$ | 3-dimensional array that represents the image stream |
| $\boldsymbol{U}_j$ | $j^{th}$ image, $j = 1, \dots, J$ |
| $u_j(m,n)(m,n)$ | element of the matrix $\boldsymbol{U}_j$, $j = 1, \dots, J$ |
| $\mathbf{V}$ | Eigenvector matrix |
| VPCA | Vectorized PCA |
| $\mathbf{x}_l$ | $l^{th}$ row of the $\mathbf{X}$ matrix, $l = 1, \dots, p$ |
| $\bar{\mathbf{x}}$ | Cross-sectional average profile of the $\mathbf{X}$ matrix |

| | |
|---|---|
| $\hat{\mathbf{x}}_l(m)$ | $l^{th}$ reconstructed profile of the $\mathbf{X}$ matrix based on $m$ retained PCs, $l = 1, \dots, p$ |
| $\mathbf{X}, \mathbf{X}_J$ | Data matrix resulting from unfolding operation |
| $\mathbf{z}_l$ | $l^{th}$ score vector of the VPCA, $l = 1, \dots, p$ |
| $\lambda_j$ | $j^{th}$ eigenvalue, $j = 1, \dots, J$ |

## REFERENCES


[1] Gibson, I., Rosen, D. W., Stucker, B. 2010. "Additive manufacturing technologies". New York: Springer.

[2] Horn, T. J., Harrysson, O. L. 2012. "Overview of current additive manufacturing technologies and selected applications". Science progress, 95(3), pp. 255-282.

[3] Mellor, S., Hao, L., Zhang, D. 2014. "Additive manufacturing: A framework for implementation". International Journal of Production Economics, 149, pp. 194-201.

[4] Olakanmi, E. O., Cochrane, R. F., Dalgarno, K. W. 2015. "A review on selective laser sintering/melting (SLS/SLM) of aluminium alloy powders: Processing, microstructure, and properties". Progress in Materials Science, 74, pp. 401-477

[5] Zhang, B., & Coddet, C. 2016. "Selective laser melting of iron powder: observation of melting mechanism and densification behavior via point-track-surface-part research". Journal of Manufacturing Science and Engineering,138(5), pp. 051001 – 05001-9.

[6] Mertens, R., Clijsters, S., Kempen, K., & Kruth, J. P. 2014. "Optimization of Scan Strategies in Selective Laser Melting of Aluminum Parts With Downfacing Areas". Journal of Manufacturing Science and Engineering, 136(6), 061012 – 061012-7.

[7] Gu, D., Chang, F., & Dai, D. 2015. "Selective Laser Melting Additive Manufacturing of Novel Aluminum Based Composites With Multiple Reinforcing Phases". Journal of Manufacturing Science and Engineering, 137(2), 021010-021010-11.

[8] Frazier, W. E. 2014. "Metal additive manufacturing: A review". Journal of Materials Engineering and Performance, 23(6), pp. 1917-1928.

[9] Zhang, L. C., Attar, H. 2015. "Selective Laser Melting of Titanium Alloys and Titanium Matrix Composites for Biomedical Applications: A Review". Advanced Engineering Materials, DOI: 10.1002/adem.201500419

[10] Chua, C. K., Leong, K. F., Liu, Z. H. 2015. “Rapid Tooling in Manufacturing”. In Handbook of Manufacturing Engineering and Technology (pp. 2525-2549). Springer London.

[11] Tapia, G., Elwany, A. 2014. “A Review on Process Monitoring and Control in Metal-Based Additive Manufacturing”. Journal of Manufacturing Science and Engineering, 136(6), pp. 060801.

[12] Mani, M., Lane, B., Donmez, A., Feng, S., Moylan, S., & Fesperman, R. 2015. “Measurement Science Needs for Real-time Control of Additive Manufacturing Powder Bed Fusion Processes”, NISTIR 8036, http://dx.doi.org/10.6028/NIST.IR.8036

[13] Craeghs, T., Bechmann, F., Berumen, S., Kruth, J.-P. 2010. “Feedback control of Layerwise Laser Melting using optical sensors”. Physics Procedia, pp. 505–514.

[14] Craeghs, T., Clijsters, S., Yasa, E., Bechmann, F., Berumen, S., Kruth, J.-P. 2011. “Determination of geometrical factors in Layerwise Laser Melting using optical process monitoring”. Optics and Lasers in Engineering, pp. 1440–1446.

[15] Clijsters, S., Craeghs, T., Buls, S., Kempen, K., Kruth, J.-P. 2014. “In situ quality control of the selective laser melting process using a high-speed, real-time melt pool monitoring system”. International Journal of Advanced Manufacturing Technologies, pp. 1089–1101.

[16] Doubenskaia, M., Pavlov, M., Grigoriev, S., Tikhonova, E., & Smurov, I. 2012. “Comprehensive Optical Monitoring of Selective Laser Melting”. Journal of Laser Micro/Nanoengineering, pp. 236-243.

[17] Lott, P., Schleifenbaum, H., Meiners, W., Wissenbach, K., Hinke, C., & Bültmann, J. 2011. “Design of an Optical system for the In Situ Process Monitoring of Selective Laser Melting (SLM)”. Physics Procedia 12, pp. 683–690.

[18] Abdelrahman, M., Starr, T. L. 2014. “Layerwise Monitoring of Polymer Laser Sintering Using Thermal Imaging”. 25th Solid Freeform Fabrication Symposium SFF 2014. Texas: Laboratory for Freeform Fabrication and University of Texas at Austin.

[19] Krauss, H., Eschey, C., & Zaeh, M. 2012. “Thermography for Monitoring the Selective Laser Melting Process”. Proceedings of the Solid Freeform Fabrication Symposium, pp. 999-1014.

[20] Jacobsmuhlen, J. z., Kleszczynski, S., Schneider, D., & Witt, G. 2013. “High resolution imaging for inspection of Laser Beam Melting systems”. Instrumentation and Measurement Technology Conference (I2MTC) (pp. 707 - 712). Minneapolis, MN: IEEE.

[21] Schilp, J., Seidel, C., Krauss, H., J.Weirather. 2014. “Investigations on Temperature Fields during Laser Beam Melting by Means of Process Monitoring and Multiscale Process Modelling”. Advances in Mechanical Engineering, 6, Article ID 217584, 7 pages.

[22] Jolliffe I. T. 2002, 2Principal Component Analysis”, 2nd Edition, Springer Series in Statistics

[23] Johnson, R. A., & Wichern, D. W. 1992. “Applied multivariate statistical analysis” (Vol. 4). Englewood Cliffs, NJ: Prentice hall.

[24] Montgomery D. C. 2008. “Introduction to Statistical Quality Control”, John Wiley & Sons, 6th Ed

[25] Hastie, T., Tibshirani, R., Friedman, J. 2009. “The elements of statistical learning” (Vol. 2, No. 1). Springer, New York

[26] Galimberti, G., Guagliano, M., Previtali, B., Rampino, L. 2015. “Digital aesthetic of new products obtained by selective laser melting processes”. Procedings of the 20th International Conference on Engineering Design, ICED15, Vol. 4, July 27-30, 2015, Milan, Italy

[27] Kiers H. A. L. 2000, “Towards a Standardized Notation and Terminology in Multiway Analysis”, Journal of Chemometrics, 14, pp. 105 - 122

[28] Yang J., Zhang D., Frangi A. F., Yang J. 2004, “Two-Dimensional PCA: A New Approach to Appearance-Based Face Representation and Recognition”, IEEE Transactions on Pattern Analysis and Machine Intelligence, 26:1, pp. 131 - 137

[29] Gottumukkal, R., Asari, V. K. 2004. “An improved face recognition technique based on modular PCA approach”. Pattern Recognition Letters, 25(4), pp. 429-436.

[30] Rodarmel, C., Shan, J. 2002. “Principal component analysis for hyperspectral image classification”. Surveying and Land Information Science,62(2), pp. 115-122.

[31] Ye J., Janardan R., Li Q. 2004, “GPCA: An Efficient Dimension Reduction Scheme for Image Compression and Retrieval”, Proceedings of the 10th ACM SIGKDD International Conference on Knowledge Discovery and Data Mining, pp. 354 – 363

[32] Nomikos P., MacGregor J. F. 1995, “Multivariate SPC Charts for Monitoring Batch Processes”, Technometrics, 37:1, pp. 41 – 59

[33] Megahed, F. M., Woodall, W. H., & Camelio, J. A. 2011. “A review and perspective on control charting with image data”. Journal of quality technology, 43(2), pp. 83-98

[34] Jäger, M., Hamprecht, F. 2009. “Principal component imagery for the quality monitoring of dynamic laser welding processes”. Industrial Electronics, IEEE Transactions on, 56(4), pp. 1307-1313.

[35] Senin, N., Ziliotti, M., & Groppetti, R. 2007. “Three-dimensional surface topography segmentation through clustering”. Wear, 262(3), pp. 395-410.

[36] Hartigan, J.A. 1975. “Clustering algorithms”. Wiley Ed., New York

[37] Ball, G.H., Hall, D.J. 1965. “ISODATA, A novel method of data analysis and pattern classification”. Tech. Rep. NTIS No. AD 699616. Standford Research Institute, Menlo Park

[38] Calinski, T., Harabasz, J. 1974. “A dendrite method for cluster analysis”. Communication in statistics, 3, pp. 1–27

[39] Zhao, Q., Xu, M., Fränti, P., 2009, “Sum-of-squares based cluster validity index and significance analysis. Adaptive and Natural Computing Algorithms”, Lecture Notes in Computer Science, 5495, pp. 313-322

[40] Xu, L. 1997. “Bayesian Ying-Yang machine, clustering and number of clusters”. Pattern Recognition Letters, 18, pp. 1167–1178

[41] Grasso, M., Colosimo, B. M., Pacella, M. 2014. “Profile monitoring via sensor fusion: the use of PCA methods for multi-channel data”. International Journal of Production Research, 52(20), pp. 6110-6135.

[42] Valle S., Li W., Qin S. J. 1999, “Selection of the Number of Principal Components: the Variance of Reconstruction Error Criterion with a Comparison to Other Methods”, Industrial & Engineering Chemistry Research, 38, pp. 4389-4401

[43] Williams, J. D., Woodall, W. H., Birch, J. B., and Sullivan, J. H. 2006, “On the Distribution of Hotelling’s T2 Statistic based on the Successive Differences Covariance Matrix Estimator”, Journal of Quality Technology, 38, pp. 217-229

[44] Colosimo, B.M., Pacella, M. 2007, “On the Use of Principal Component Analysis to Identify Systematic Patterns in Roundness Profiles”, Quality and Reliability Engineering International, 23, pp. 925 - 941

## APPENDIX A: OVERVIEW OF THE VPCA TECHNIQUE

The first step of the VPCA [32 - 34, 41] consists of performing a spectral decomposition,

$\mathbf{V}^T\mathbf{S}\mathbf{V} = \mathbf{L}$, of the sample variance-covariance matrix $\mathbf{S} \in \mathbb{R}^{J\times J}$ of the $p \times J$ data matrix $\mathbf{X}$. $\mathbf{L}$ is a diagonal matrix whose diagonal elements are the eigenvalues of $\mathbf{S}$ ($\lambda_j$; $j = 1, \dots, J$), and $\mathbf{V}$ is an orthonormal matrix whose $j^{th}$ column, $\boldsymbol{v}_j$, is the $j^{th}$ eigenvector of $\mathbf{S}$.[6] The projection of the $l^{th}$ pixel intensity profile onto the $J$-dimensional PC orthogonal space is defined as follows (a.k.a. "score"):

$$\mathbf{z}_l = \mathbf{V}^T(\mathbf{x}_l - \bar{\mathbf{x}}) = \left[z_{l,1}, \dots, z_{l,J}\right]^T \qquad (l = 1, \dots, p = M \times N) \tag{A1}$$

where $\mathbf{x}_l = \boldsymbol{u}(m,n) = \left[u_1(m,n), \dots, u_J(m,n)\right]^T$ is the $l^{th}$ row of the data matrix $\mathbf{X}$ and $\bar{\mathbf{x}} = (1/p)\sum_{l=1}^{p}\mathbf{x}_l$ is the cross-sectional average profile among the $p$ intensity profiles used to estimate the VPCA model. Extracted PCs are linear combination of frames from $j = 1$ to $j = J$. This means that the $j^{th}$ eigenvector, $\boldsymbol{v}_j$, contains the weights, a.k.a. "loadings", of this linear combination. The first PC is the maximum variance linear combination; the second PC is the maximum variance linear combination having zero-correlation with the first one; and so on. The relative importance of each PC, i.e. the amount of explained variance, is represented by the value of the corresponding eigenvalue. Thus, the relevant information enclosed in the image stream may be captured by a reduced number of PCs, say $m$. The number $m$ of relevant PCs can be selected by

[6] For process monitoring applications the variance-covariance matrix estimation based on the successive difference operator is advocated [43].

setting a threshold on the minimum percentage of overall data variance explained by those PCs. This method guarantees that PCs retained from iteratively generated matrices actually refer to the same amount of data variability. Other methods have been proposed in the literature: for a comparison study see Valle *et al*. [42].

In order to characterize the behaviour of each pixel and to identify single pixels (or spatial clusters of pixels) that exhibit anomalous intensity profiles, the Hotelling's $T^2$ statistic can be used:

$$T_l^2 = \sum_{j=1}^{m} \frac{z_{l,j}^2}{\lambda_j} \qquad (l = 1, \dots, p = M \times N) \tag{A2}$$

Contrary to profile monitoring applications [41, 44], in our proposed approach, $T_l^2$ is a spatial indicator through the mapping $T_l^2 \in \mathbb{R}_+^p \rightarrow T^2(X,Y) \in \mathbb{R}_+^{M \times N}$, and hence it can be represented in the same domain of original images, $T^2(X,Y)$, where $X$ and $Y$ denotes the image pixel location. The spatial distribution of $T^2(X,Y)$ is therefore suitable to synthetize the information content of a video, represented in terms of a 3-dimensional array, into a spatially distributed descriptor. Usually it is advocated to couple the Hotelling's $T^2$ statistic with an additional statistic that allows one to monitor patterns that affect directions orthogonal to the ones associated to the retained PCs. Such a statistic is known as "squared prediction error" (SPE) and it involves the estimation of the reconstructed intensity profiles. By retaining the first $m$ PCs, each pixel intensity profile, i.e. each row of the matrix $\mathbf{X}$, may be reconstructed as follows:

$$\hat{\mathbf{x}}_l(m) = \bar{\mathbf{x}} + \sum_{j=1}^{m} z_{l,j} \boldsymbol{v}_j \qquad (l = 1, \dots, p = M \times N) \tag{A3}$$

Then, the SPE statistic is given by:

$$SPE_l = (\hat{\mathbf{x}}_l(m) - \bar{\mathbf{x}})^T(\hat{\mathbf{x}}_l(m) - \bar{\mathbf{x}}) \qquad (l = 1, \dots, p = M \times N) \qquad \text{(A4)}$$

Analogously to the $T_l^2$ indicator, the $SPE_l$ is a spatial statistic through the mapping $SPE_l \in \mathbb{R}_+^p \rightarrow SPE(X,Y) \in \mathbb{R}_+^{M \times N}$. If a defect affects the pixel intensity profiles in a way that is not captured by the retained PCs, the SPE statistic guarantees that no information is lost, and the defect might be localized by looking at high values of $SPE(X,Y)$. This study focused on the $T^2(X,Y)$. Future development may be aimed at extending the k-means clustering methodology to include the $SPE(X,Y)$ descriptor, too, into the analysis.

## APPENDIX B: ON THE PHYSICAL INTERPRETATION OF PCS

The physical understanding of estimated PCs plays a key role to interpret the results of the proposed approach. Here a discussion about the analysis of triangle 1 is briefly presented. Analogous conclusions can be drawn for other image streams. Fig. B1 shows the loadings of $m = 12$ retained PCs that explain the 80% of the overall image stream variability. Each loading, $\boldsymbol{v}_j$, is a vector of length $J$ that associates a weight to each frame. Thus, contrary to the traditional VPCA for image analysis, the loadings in our proposed approach are linear combinations of points in time (i.e., the frames). The effects of the overheating of corner C were mainly visible during the time window that is marked by red dotted lines in Fig. B1. The PCs that associate a larger weight to points in time within that time window are the first three PCs. Thus, they represent the most informative variables for defect detection.

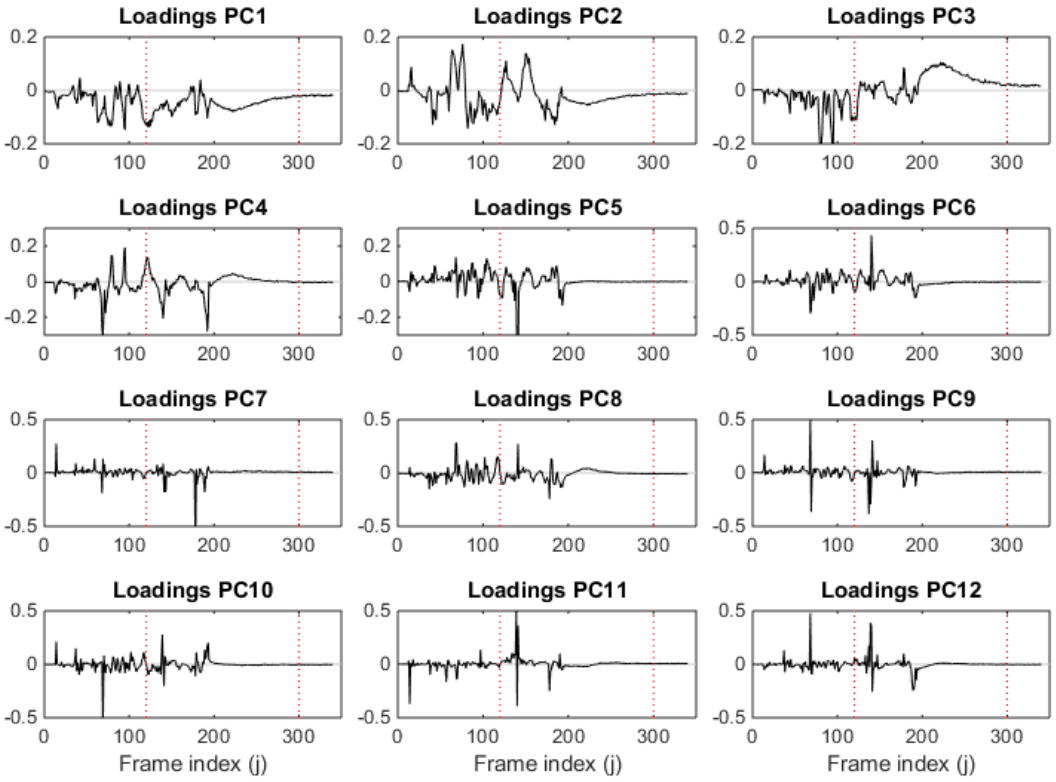


Fig. B1 - Loadings of retained PCs estimated by analysis the entire image stream for triangle 1 (red dotted lines mark the time window during which the overheating effects of corner C were visible)

The scores corresponding to these retained PCs are vectors of real numbers in $\mathbb{R}^p$, and hence they can be represented via the mapping $\mathbb{R}^p \rightarrow \mathbb{R}^{M \times N}$. Fig. B2 shows the spatial distribution of the scores corresponding to the loadings in Fig. B1. Each score value, $z_{l,j}$, represents the projection of the $l^{th}$ pixel, $l = 1, \ldots, p = M \times N$, onto the $j^{th}$ PC, $j = 1, \ldots, m$. Fig. B2 shows that, along the first principal direction, the defect is visible as a contrast between the acute corner C and the background area. Along the second principal direction, the defect is visible as a contrast between corner C and the opposite corner A. Along the third principal direction, the defect is visible as a contrast between

corner C and the surrounding area. Therefore, in this study the effects of the local defect is visible along the first three PCs, whereas following PCs provide a limited contribution. Generally speaking, in case a defect is such that its effects are only visible along directions that are orthogonal to those PCs, an additional statistic, i.e., the $SPE(X,Y)$, is required to avoid information losses. As an example, the $SPE(X,Y)$ spatial distribution for triangle 1 is shown in Fig. B3. Analogously to the $T^2(X,Y)$ indicator, the $SPE(X,Y)$ exhibits larger values corresponding to the down-facing acute corner C, but it provides no significant additional information.

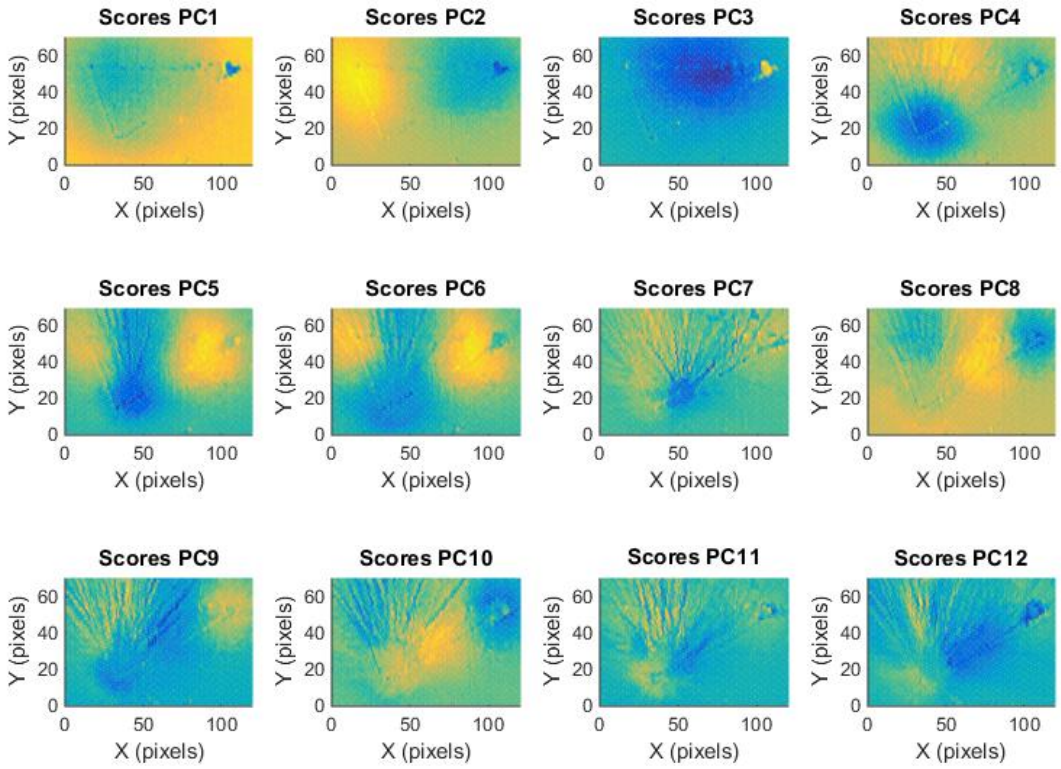


Fig. B2 - Scores of retained PCs estimated by analysis the entire image stream for triangle 1

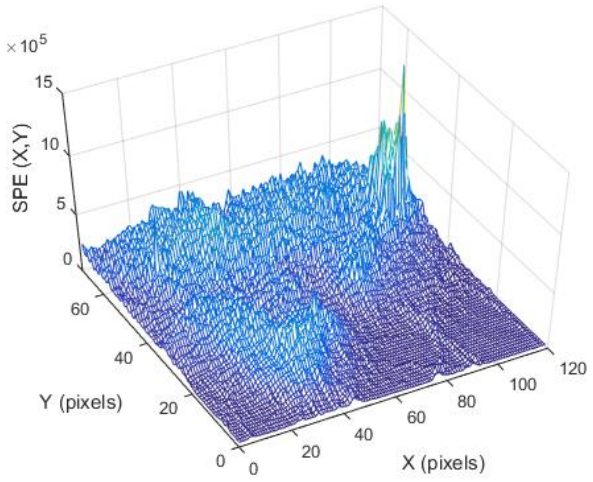


Fig. B3 - 3D representation of the $SPE(X,Y)$ statistic triangle 1; the colour map ranges from dark blue (lower values) to bright yellow (larger values); see the on-line version of the paper for color figures